



Ply-Resolved Quantification of Thermal Degradation in Carbon Fibre-reinforced Polymers

Johannes Bibinger^{1,2} , Sebastian Eibl²  and Hans-Joachim Gudladt¹

Abstract

This study focuses on thermal degradation of carbon fibre-reinforced polymers depending on the specimen depth. For this purpose, the commercial composite HexPly® 8552/IM7 was thermally irradiated from one side with an infrared lamp at constant heat flux of 50 W/cm² under varying exposure time. Subsequently, a defined number of plies was removed to prepare micro samples from different depths of the bulk material. Non-destructive and destructive testing methods were used to characterize the thermal degradation mechanism and mechanical properties of these specimens. The results showed that during thermal loading temperature and consequently damage gradients manifest along the material cross-section. Thereby, the damage distribution could be divided into the regions r_I with matrix depletion, r_{II} with and r_{III} without structural damage such as delaminations, cracks and pores. By means of ply-resolved investigations, the influence of these regions and corresponding decomposition processes on the mechanical properties could be determined. As a result, a simple damage model was introduced to calculate the residual strength from the initial strength, region sizes and sensitivity factors representing the effect of thermo-induced damage on strength types.

Keywords

One-sided thermal loading, ply profile, degradation mechanism, mechanical properties, three-region model

Introduction

CFRP are composite materials with high specific strength and stiffness.^{1–3} Due to these mechanical properties, they are indispensable for lightweight structures in the aerospace industry.^{4–6} Unfortunately, these composites also exhibit lower thermal stability compared to metallic structures.^{7–11} Nevertheless, to ensure safe application, thermal threats and their effects on the decomposition mechanism and properties of the material must be known. In this case, threats such as fully developed fires (heat flux $q = 5$ W/cm²),¹² burning fuels and propellants ($q = 15 - 20$ W/cm²)¹³ as well as detonations ($q = 50$ W/cm²)¹³ must be expected for military aircraft. Characteristic for these scenarios are the one-sided thermal loads under formation of temperature and damage gradients along the material cross-section.^{14,15} Thereby, the resulting decomposition processes and damage distributions depend on the heat flux and irradiation time.¹⁴

Until now, scientific investigations primarily concentrate on low heat fluxes.^{15–17} During these thermal irradiations, the composite is heated moderately. For example, at a heat flux of 5 W/cm², the material heated up with ~4 °C/s after

short warm-up interval.¹⁵ As a result, surface temperatures of only ~350 °C were reached in one minute. Thereby, the temperature between front and back side differed less than $T < 150$ °C, resulting in relatively homogeneous damage behavior over the 4 mm material cross-section.¹⁵ In contrast, at high heat fluxes $q \geq 50$ W/cm², these temperatures and temperature gradients were exceeded within seconds.¹⁴ Consequently, thermal degradation processes such as thermo-oxidative damage, weakening of fibre-matrix adhesion, degradation of polymeric matrix and carbon fibres, formation of delaminations, cracks, pores as well as matrix depletion occurred abruptly.^{14,18} Since these processes arise

¹University of the Bundeswehr Munich – Institute for Material Science, Neubiberg, Germany

²Bundeswehr Research Institute for Materials, Fuels and Lubricants (WIWeB), Erding, Germany

Corresponding author:

Johannes Bibinger, University of the Bundeswehr Munich – Institute for Material Science, Werner-Heisenberg-Weg 39, Neubiberg 85577, Germany.

Email: Johannes.Bibinger@unibw.de

in combination with extreme damage gradients, the material properties depend significantly on the specimen depth.¹⁴

For this reason, the unidirectional composite 8552/IM7 has been irradiated with an infrared lamp at 50 W/cm² from one side under varying irradiation time. To analyze the thermo-induced damage gradient, a defined number of plies was removed to prepare micro samples in different depths of the bulk material. Subsequently, the bulk and micro samples were investigated using non-destructive and destructive methods. The aim of this study is to characterize, classify and quantify the thermal damage in order to determine its effect on the mechanical properties. For this purpose, the material cross-section was separated into three regions with different damage states. These consisted of the regions r_I with matrix depletion as well as r_{II} with and r_{III} without structural damage such as delamination, cracks and pores. By means of depth profiles the effect of degradation processes as well as damage regions on residual strength could be determined. It turned out that the mechanical loading types react differently sensitive to these regions. Consequently, residual interlaminar shear, compressive, flexural and tensile strengths were affected variously from, e. g., delaminations. However, since experimental residual strengths correlate with calculated residual strengths, a three-region model could be introduced. In this model, residual strength was calculated from the product sum of initial strengths, region sizes and sensitivity factors, representing the effect of thermo-induced damage on strength types.

Experimental

Sample preparation and treatment

In this research, the commercially available CFRP HexPly[®] 8552/IM7 from Hexcel Composites GmbH (Stade, Germany) was used. The initial material consisted of prepregs with unidirectional carbon fibres impregnated in epoxy resin system.¹⁹ HexTow[®] IM7 are continuous, intermediate modulus, polyacrylonitrile based fibres with a filament count of 12K.²⁰ HexPly[®] 8552 is a high-performance cured matrix, composed of the epoxy components tetraglycidyl methylene dianiline as well as triglycidyl-p-aminophenol, the curing agent 3,3'- or 4,4'-diaminodiphenyl sulfone and the thermoplastic toughener polyethersulfone.^{21,22} According to the manufacturer's data sheet, the glass transition temperature of the cured dry matrix is $T_g = 200$ °C.¹⁹

32 plies of 8552/IM7 prepregs were laminated to unidirectional 500 × 500 mm² panels and cured according to the manufacturer's specifications.¹⁹ With a nominal cured ply thickness of 0.131 mm,¹⁹ approximately $d_1 = 4$ mm thick laminates were formed. Referring to the data sheets, the cured composite has an 0° interlaminar shear strength of $\tau = 137$ MPa, 0° compressive strength of $\sigma_c = 1690$ MPa, 0°

flexural strength of $\sigma_f = 1860$ MPa and 0° tensile strength of $\sigma_t = 2538$ MPa.^{19,23}

In addition, 100 × 100 mm² panels were manufactured with inserted type K thermocouples.²⁴ To evaluate the temperature as a function of sample depth, eight thermocouples were centrally laminated between 3–4, 7–8, 11–12, 15–16, 19–20, 25–26 plies and additionally positioned on the front and back side using peel ply. Thereafter, the thermocouple-equipped panels were cured in an autoclave according to the manufacturer's recommendations.¹⁹

With the ultrasonic testing system Hill-Scan 3060 UHF from Dr. Hillger (Braunschweig, Germany), the material was inspected for quality defects such as pores, macroscopic delaminations and fibre orientation defects according to DIN EN ISO 16810.²⁵ A test head from Panametrics with a frequency of 15 MHz and a step size of 0.1 mm was used. After quality control, with the exception of 130 × 100 and 330 × 100 mm² for some compressive and tensile strength samples, only 100 × 100 mm² panels were cut with a water-cooled diamond wheel saw and dried for one week in a heating chamber with forced convection at $T = 70$ °C until mass constancy.

Subsequently, the 3000 W infrared lamp from Micor's tube emitter (Niedernhausen, Germany) was adjusted to a heat flux of $q = 50$ W/cm² at 25 mm distance using a heat flux meter of Fire Testing Technology's cone calorimeter. The panels were thermally loaded from one side with varying time intervals of $t_1 = 5, 10, 15, 20, 25$ and 30 s (see schematic representation in Figure 1(a)). Thereby, the irradiation energy impinges homogeneously on the surface over a width of $\Delta y = 100$ mm and minimum height of $\Delta x = 20$ mm. During thermal loading, the temperature was recorded with the TC-08 data logger from pico Technology.

Furthermore, Figure 1(b) schematically shows the preparation of bulk and micro specimens. First, sample strips with defined length and width were cut from the panels. Part of these strips with 32 plies were used directly and denoted as bulk specimens. For the other strips, a defined number of plies were removed from the back and front side using a pendulum grinding machine to produce thinner samples with 16 or 8 plies in different depths, designated as micro specimens. Thereby, the preparation and counting of the removed plies always started from the back side. An overview of the bulk and micro samples with specification of irradiation times and ply ranges can be taken from Table 1.

Non-destructive testing

By means of micro attenuated total reflection Fourier transform infrared spectroscopy (ATR-FTIR), matrix degradation depending on the ply depth can be quantified.^{21,26} For this, inclines with an angle of 11.3° were ground along the width of 40 × 20 mm² bulk samples. With the infrared

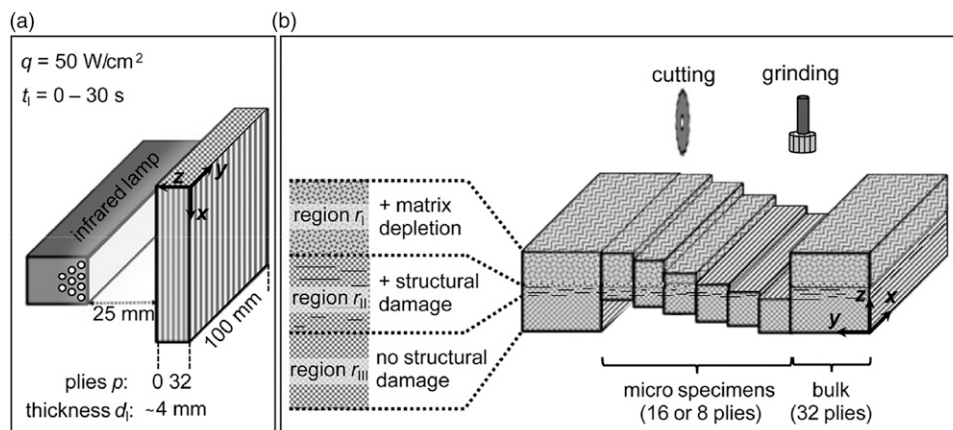


Figure 1. Schematic representation of (a) one-sided thermal irradiation of a CFRP panel with an infrared lamp and (b) preparation of micro specimens from bulk material as well as classification of damage regions r_i .

microscope LUMOS II from Bruker, 10 average spectra per ply with a depth resolution of $\Delta z \sim 40 \mu\text{m}$ were recorded in a wavenumber range of $\tilde{\nu} = 4000 - 400 \text{ cm}^{-1}$ using a germanium crystal and thermoelectric MCT detector.

Dynamic mechanical analysis (DMA) can be used to measure the storage modulus. Thereby, $60 \times 10 \text{ mm}^2$ micro and bulk specimens were tested with three-point bending setup according to DIN EN ISO 6721-1 using Gabo Eplexor[®] 500 from Netzsch.²⁷ These samples were heated from $T = 30 - 275 \text{ }^\circ\text{C}$ with a heating rate of $\theta = 1 \text{ }^\circ\text{C}/\text{min}$. Simultaneously, static load of 10% and dynamic load of 5% from the specimen cross-section strain was applied at a frequency of $f = 1 \text{ Hz}$.

The sample density was examined with the CM224S balance from Sartorius (Goettingen, Germany) and the equipped hydrostatic density determination set using the Archimedes principle according to DIN EN ISO 1183-1.²⁸ In this regard, the sample masses were measured in air and water atmosphere to obtain the density of the material.

Thermally induced defects such as delaminations, cracks and pores could be visualized with the micro-focused computed X-ray tomograph (μCT) V-TOME XL 300 from General Electric. A 180 kV source was used to record the volumes of $40 \times 20 \text{ mm}^2$ bulk samples and sliced into two x - y images per ply with voxel size of $10 \mu\text{m}$. In the tomograms, the damaged area of CFRP can be identified, because the contained air and pyrolysis gases in the defects reduce the X-ray attenuation and thus displayed in darker gray levels.^{29,30} To quantify the damaged area, the number of voxels and their gray levels were determined. The threshold value for the gray level defining the damaged material was set by successively increasing the threshold until the deepest defects were just detected. The percentage damaged area represents the ratio between the number below the threshold and the total number of voxels in x - y plain. Similarly, the percent damaged volume could be

determined, when gray scale analysis was applied to multiple plies.

Destructive testing

The apparent interlaminar shear strength of composite materials was determined with short beam shear tests using a universal testing machine Z020 from Zwick/Roell in accordance to DIN EN ISO 2563.³¹ The specimens were positioned with the irradiated side on the two lower supports and tested at a constant rate of $1 \text{ mm}/\text{min}$. For $40 \times 20 \text{ mm}^2$ bulk specimens, supports with 5 mm radius, support distance of 20 mm and a 25 kN loading cell of type Xforce P from Zwick/Roell were used. For $20 \times 10 \text{ mm}^2$ micro samples, support radius of 3 mm , support distance of 10 mm and a 5 kN loading cell of the same type were utilized.

Compressive strength of the specimens was assessed with the universal testing machine Z250 from Zwick/Roell in accordance to DIN EN ISO 14126.³² For this purpose, $64 \times 10 \text{ mm}^2$ and $45 \times 10 \text{ mm}^2$ glass fibre tabs were glued to both ends of $140 \times 10 \text{ mm}^2$ bulk and $100 \times 10 \text{ mm}^2$ micro samples, respectively, using the universal two-component epoxy resin adhesive Delo-Duopox[®] 1895 according to the manufacturer's instructions.³³ The specimens were tested in Celanese fixture at a constant rate of $1 \text{ mm}/\text{min}$ using a 250 kN loading cell of the type Xforce K from Zwick/Roell.

By means of 4-point flexural test, the flexural strength of the samples was evaluated with the universal testing machine Z020 from Zwick/Roell in accordance to DIN EN ISO 14125.³⁴ The thermally irradiated side of $100 \times 15 \text{ mm}^2$ bulk and micro samples rested on the lower supports. Flexural strength was tested at $5 \text{ mm}/\text{min}$ with support radius of 2 mm , support distance of 81 mm and a 5 kN loading cell of the type Xforce P from Zwick/Roell.

Tensile strength of the composites was obtained with the Z250 universal testing machine from Zwick/Roell

Table 1. Sample list with irradiation times t_i , ply ranges p_r , distributions of damage regions r_i as well as residual strengths together with the occurring damage phenomena s = shear failure, sd = shear failure with ductile behavior, cf = compressive failure, c = crack and b = brooming.

Strength type	Ply range $p_r / -$	Irradiation time t_i / s																				
		0			5			10			15			20			25			30		
		r_i	r_{ii}	r_{iii}	r_i	r_{ii}	r_{iii}	r_i	r_{ii}	r_{iii}	r_i	r_{ii}	r_{iii}	r_i	r_{ii}	r_{iii}	r_i	r_{ii}	r_{iii}	r_i	r_{ii}	r_{iii}
Int. Shear strength / MPa	0-16	118	s	70	s	42	s	21	sd	—	—	—	—	—	—	—	—	—	—	—	—	—
	2-18	122	s	82	s	57	s	30	s	—	—	—	—	—	—	—	—	—	—	—	—	—
	4-20	124	s	99	s	77	s	49	s	25	sd	—	—	—	—	—	—	—	—	—	—	—
	8-24	123	s	121	s	110	s	62	s	38	sd	24	sd	—	—	—	—	—	—	—	—	—
	12-28	122	s	121	s	102	s	85	s	49	s	29	sd	21	sd	—	—	—	—	—	—	—
	16-32	112	s	114	s	116	s	99	s	69	s	39	sd	28	sd	—	—	—	—	—	—	—
	0-32	114	s	92	s	68	s	51	s	33	sd	20	sd	16	sd	—	—	—	—	—	—	—
	0-16	1163	cf	923	b/cf	364	b/cf	247	b/cf	108	b	68	b	44	b	—	—	—	—	—	—	—
	2-18	1029	cf	979	b/cf	561	b/cf	364	b/cf	188	b	106	b	64	b	—	—	—	—	—	—	—
	4-20	1137	cf	1059	b/cf	843	b/cf	455	b/cf	271	b/cf	143	b	80	b	—	—	—	—	—	—	—
Compressive strength / MPa	8-24	1192	cf	1101	cf	1000	b/cf	843	b/cf	409	b/cf	250	b/cf	146	b	—	—	—	—	—	—	—
	12-28	1011	cf	1156	cf	1169	cf	977	cf	532	b/cf	300	b/cf	199	b	—	—	—	—	—	—	—
	16-32	1196	cf	1059	cf	1206	cf	1100	cf	714	cf	420	b/cf	318	b/cf	—	—	—	—	—	—	—
	0-32	992	cf	857	cf	688	b/cf	459	b/cf	271	b/cf	139	b/cf	112	b/cf	—	—	—	—	—	—	—
	0-16	1637	cf	1147	b/cf	886	b/cf	624	b/cf	224	b/cf	136	b	111	b	—	—	—	—	—	—	—
	2-18	1743	cf	1474	b/cf	1334	b/cf	1097	b/cf	550	b/cf	184	b	171	b	—	—	—	—	—	—	—
	4-20	1745	cf	1693	cf	1467	b/cf	1169	b/cf	763	b/cf	629	b/cf	175	b	—	—	—	—	—	—	—
	8-24	1814	cf	1677	cf	1406	cf	1360	b/cf	773	b/cf	859	b/cf	406	b/cf	—	—	—	—	—	—	—
	16-32	1527	cf	1417	cf	1527	cf	1422	cf	1397	cf	1349	b/cf	117	b/cf	—	—	—	—	—	—	—
	0-32	1420	cf	1231	b/cf	963	b/cf	700	b/cf	558	b/cf	355	b/cf	318	b/cf	—	—	—	—	—	—	—
Tensile Strength / MPa	0-8	1959	c	1081	b/c	414	b	152	b	146	b	42	b	24	b	—	—	—	—	—	—	—
	2-10	1762	c	1994	b/c	775	b/c	472	b	548	b	129	b	34	b	—	—	—	—	—	—	—
	4-14	1791	c	2195	c	1452	b/c	1018	b/c	724	b	243	b	115	b	—	—	—	—	—	—	—
	8-16	1906	c	1821	c	1756	c	1752	b/c	1765	b/c	1765	b/c	481	b	—	—	—	—	—	—	—
	12-20	2142	c	1692	c	1611	c	1834	c	1905	b/c	1139	b/c	878	b	—	—	—	—	—	—	—
	24-32	1972	c	1799	c	1875	c	1895	c	2239	c	1851	c	1599	c	—	—	—	—	—	—	—
	0-32	2310	c	2207	b/c	2028	b/c	1787	b/c	1594	b/c	1289	b/c	1035	b/c	—	—	—	—	—	—	—

according to DIN EN 2561.³⁵ The $330 \times 15 \text{ mm}^2$ bulk and $100 \times 10 \text{ mm}^2$ micro specimens were glued at both ends with $115 \times 15 \text{ mm}^2$ and $30 \times 10 \text{ mm}^2$ glass fibre tabs according to the manufacturer's specifications.³³ The measurement was performed at 2 mm/min with a 250 kN loading cell of the type Xforce K from Zwick/Roell.

Results and discussion

Characterization of thermal damage

When CFRP are thermally loaded from one side, radiation impinges on the sample surface, causing primarily reflection, emission and absorption.³⁶ Thereby, the absorbed heat is conducted in the material, visualized by temperature rises in different ply depths. For this purpose, Figure 2(a) shows temperature–time profiles $T(t)$ for heating at $q = 50 \text{ W/cm}^2$ up to 30 s as well as cooling thereafter at $q = 0 \text{ W/cm}^2$. After a very short warm-up phase, the front side heats up with a nearly constant heating rate of $\theta \sim 150 \text{ }^\circ\text{C/s}$ to $t \leq 5 \text{ s}$. With rising exposure time and temperature, the heating rate slows down. Maximum surface temperatures of approximately $T \sim 1000 \text{ }^\circ\text{C}$ are reached after $t \sim 15 \text{ s}$. Since the absorbed heat diffuses from the front to the back side, temperature gradients in z -direction can be found. Thereby, discontinuous $T(t)$ curves can arise due to impaired heat conduction along the material cross-section caused, for example, by the formation of delaminations (see $p = 7-8$).¹⁴ For $t > 30 \text{ s}$, no more radiation impinges on the sample surface. As a result, on the one hand, heat is emitted on the front side indicated by the pronounced temperature per time drop. On the other hand, heat is conducted to the back side

until the temperature gradient is reduced with rising time according to the heat conduction equation.³⁷ Consequently, continued heating and thermal damage occurs in deeper plies after the infrared lamp is switched off.^{38,39}

In addition, Figure 2(b) illustrates temperature–depth profiles $T(p)$ in z -direction for different times t . Due to the high heat flux, the material heats up very quickly, resulting in extreme temperature gradients within the first seconds. The maximum temperature difference between front and back side of $\Delta T = 814 \text{ }^\circ\text{C}$ is reached after 15 s. Within approximately 8 s, the sample ignites because sufficient pyrolysis gases are accumulated on the surface and burns until no more radiation impinges.⁴⁰ Thereby, the combustion of the sample surface reduces the absorbed heat share and a dynamic equilibrium sets in on the front side, visualized by a constant $T(t > 15 \text{ s})$ -surface profile.^{37,40} As a result, the heat flux in z -direction and consequently the temperature gradient according to the heat conduction decreases.^{37,40} Thus, temperature gradients and stress along the material cross-section increase until the maximum specimen temperature is achieved.

When CFRP are exposed to one-sided thermal irradiation, structural damage such as delaminations, pores and cracks can occur. These defects can be visualized with μCT because the containing air or pyrolysis gases reduce the X-ray attenuation more than the composite material and thus appear darker in the tomograms.^{29,30} For illustration, Table 2 shows tomograms from the structural damage gradients in z -direction at different irradiation times t_i . Generally, the damage distribution can be divided into three regions. In region r_{III} , close to the back side, no visible structural defects can be detected. In region r_{II} ,

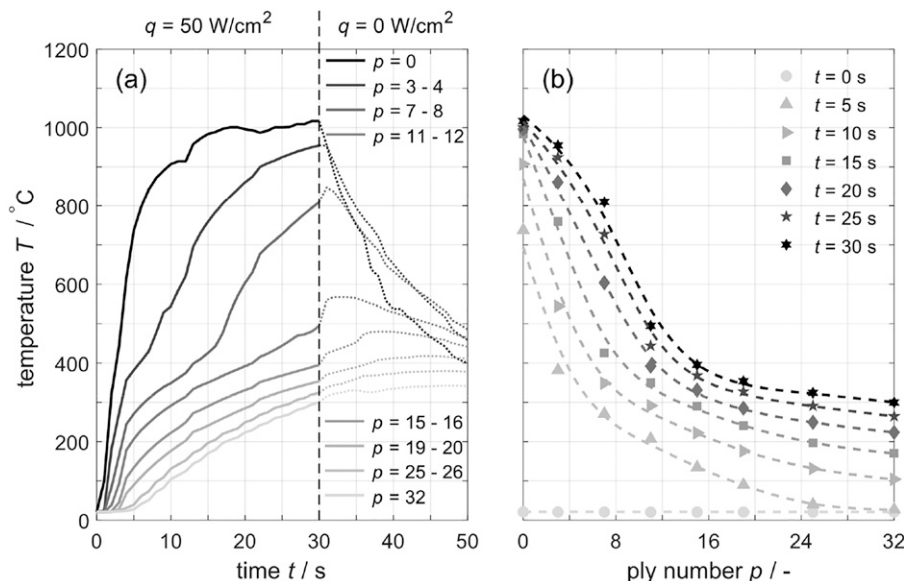


Figure 2. Temperature profiles during one-sided thermal irradiation at $q = 50 \text{ W/cm}^2$ to $t \leq 30 \text{ s}$ and cooling thereafter at $q = 0 \text{ W/cm}^2$ depending on (a) time $T(t)$ as well as (b) ply number $T(p)$ in z -direction recorded in eight different laminate depths.

Table 2. Visualization of the damage regions by μ CT: r_I with matrix depletion, r_{II} with structural damage and r_{III} without structural damage. In addition, thickness d and density ρ of the samples as well as ply numbers of damage regions $p(r_i)$ are displayed.

Time t_i	0 s	5 s	10 s	15 s	20 s	25 s	30 s
q, t_i	$\rho(r_i) = 32$ fibres 2.0 mm r_{III}	41 27 r_I r_{III}	8 3 21 r_I r_{II} r_{III}	10 7 15 r_I r_{II} r_{III}	13 12 7 r_I r_{II} r_{III}	15 17 r_I r_{II}	19 13 r_I r_{II}
d / mm	4.06 ± 0.03	4.34 ± 0.05	4.49 ± 0.03	4.74 ± 0.05	4.98 ± 0.02	5.28 ± 0.04	5.48 ± 0.03
$\rho / \text{g cm}^3$	1.593	1.579	1.542	1.529	1.478	1.427	1.363

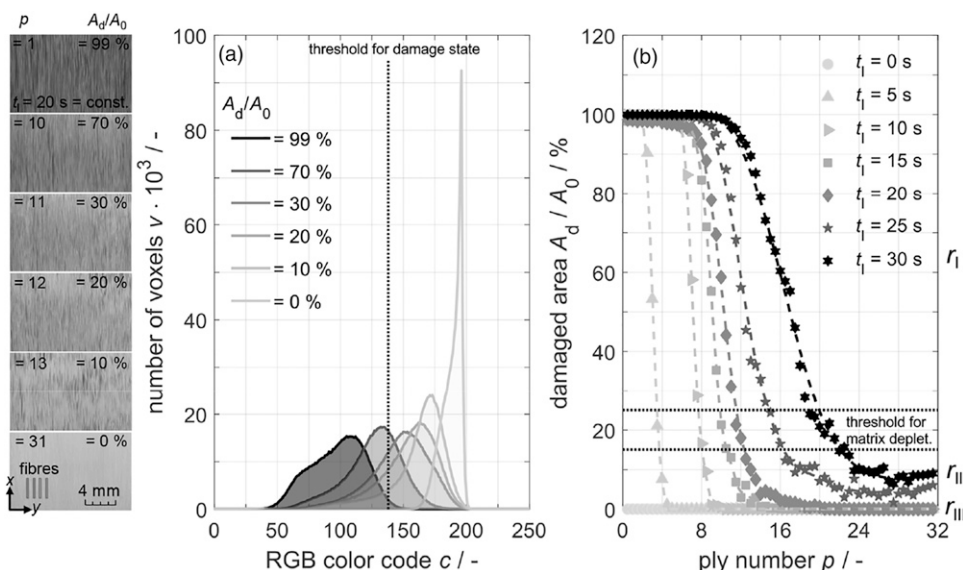


Figure 3. Determination of (a) voxel number v and RGB color code c in x - y plane of μ CT tomograms at constant irradiation time $t_i = 20$ s and varying ply number p as well as (b) damaged area A_d/A_0 depending on the ply number. In addition, threshold for matrix depletion at $A_d/A_0 \geq 20 \pm 5 \%$ and damage regions r_i are presented.

delaminations caused by thermo-induced stress along the cross-section in combination with decomposition processes of the polymeric matrix become visible. In this region, the epoxy resin decomposition temperature of about 270°C is exceeded, determined by thermogravimetric analysis at 10°C/min under oxygen atmosphere.¹⁴ In region r_I , the matrix is additionally depleted, indicated by pyrolysis gas and air inclusions. Thereby, the polyethersulfone decomposition temperature of approximately 510°C is reached, measured under identical conditions.¹⁴ Consequently, the decomposition temperatures and corresponding regions can also be inferred from the $T(p)$ curves in Figure 2(b). Furthermore, the matrix depletion in region r_I can lead to the loss of interlaminar ply adhesion and thus to expansion along the cross-section. The tomograms in Table 2 visualizes that, for example, at $q = 50 \text{ W/cm}^2$ and $t_i = 30 \text{ s}$, the relative thickness increases by 35 %. As a result, the depth

profiles refer to the number of plies and not to the depth in mm (see also schematic micro sample thicknesses and damage regions in Figure 1(b)).

To determine the structural damage along the cross-section, tomograms are generated in the x - y plane. Illustrative tomograms are shown in Figure 3 at constant irradiation time of $t_i = 20 \text{ s}$ and different ply depths p . Basically, the defects are oriented in fibre direction and increase in number and size towards the front side. With the help of gray value analysis, these defects can be quantified. For this purpose, Figure 3(a) shows the voxel number v with the corresponding RGB color code c . The RGB color code can assume values between black (red = 0, green = 0, blue = 0) and white (255, 255, 255).⁴¹ Since these values change uniformly for red, green, and blue in gray scale analysis, the RGB color code is simplified from black to white with $c = 0\text{--}255$.⁴¹ In the initial state, no defects are

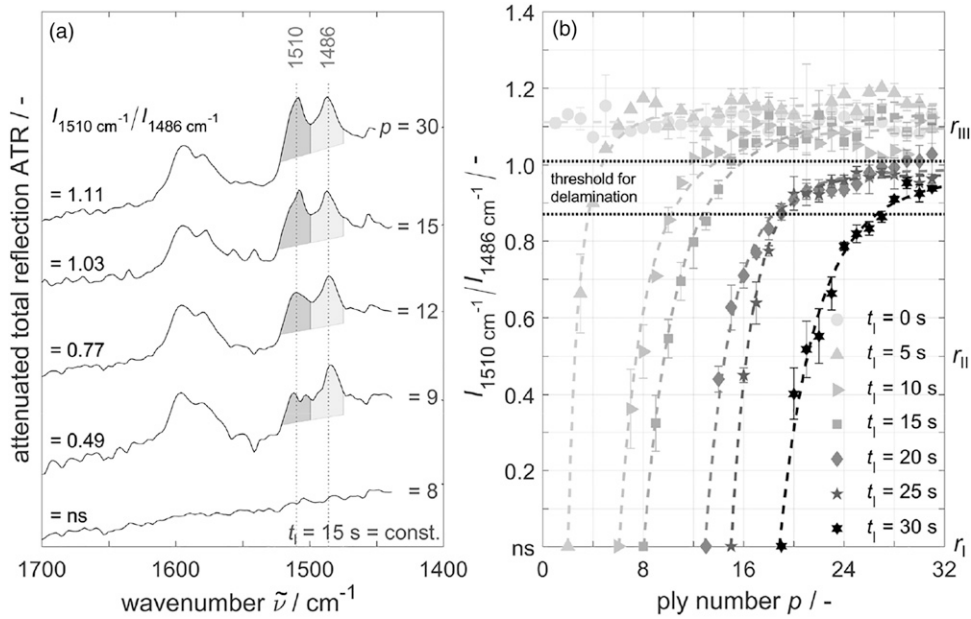


Figure 4. Determination of (a) band intensities at $\tilde{\nu} = 1510$ and 1486 cm^{-1} from vertically shifted infrared spectra at constant irradiation time $t_i = 15 \text{ s}$ recorded towards the front side as well as (b) intensity ratio $I_d = I_{1510 \text{ cm}^{-1}}/I_{1486 \text{ cm}^{-1}}$ in relation to ply number p after various irradiation times t_i . In addition, threshold for delaminations at $I_d = 0.94 \pm 0.07$, depth without infrared signal (ns) and damage regions r_i are given.

visible, resulting in high color codes with a narrow color distribution. With growing structural damage, lower color codes and a broader distribution occurs. By introducing a threshold for damaged material, the percentage damaged area A_d/A_0 can be determined. A_d represents the number of voxels below the threshold and A_0 the total number of voxels. Figure 3(b) shows this damaged area for different irradiation times along the ply depth. At $q = 50 \text{ W/cm}^2$, extreme structural damage gradients occur within a few seconds. Thereby, the damage distribution can be separated into three regions. In region r_{III} , no structural damage is present with $A_d/A_0 = 0 \%$. Only with the presence of region r_{II} , thermo-induced delaminations can be detected. The ply depth at the transition from r_{III} to r_{II} thus represent the border for delamination formation. In region r_{I} , the polymeric matrix is additionally depleted, confirmed by the density loss from 1.593 to 1.363 g/cm^3 within $t_i = 30 \text{ s}$ in Table 2. The transition between r_{II} and r_{I} hence constitutes the threshold for matrix depletion at $A_d/A_0 = 20 \pm 5 \%$, determined by infrared spectroscopy in Figure 4(b) and explained in the following paragraphs. Based on this region classification with μCT , the bulk with 32 plies can be separated into $p(r_{\text{III}}) = 21$ plies without and $p(r_{\text{II}}) = 3$ plies with structural damage as well as $p(r_{\text{I}}) = 8$ plies with matrix depletion after a thermal exposure of, e. g., $t_i = 10 \text{ s}$ (see also Table 2).

The thermal degradation of the polymeric matrix can be detected with the help of FTIR. For illustration, infrared spectra are shown in Figure 4(a) at constant exposure time of $t_i = 15 \text{ s}$ and different ply depths p . In these spectra, the band at $\tilde{\nu} = 1510 \text{ cm}^{-1}$ can be assigned to the C–C stretching

vibration of the aromatic ring structure from the epoxy resin.^{21,22} Whereas, the band at $\tilde{\nu} = 1486 \text{ cm}^{-1}$ can be assigned to the C–C stretching vibration of the aromatic ring structure from polyethersulfone.^{21,22} Towards the front side, the band intensity of the epoxy resin reduces due to its low thermal stability (see dark gray area).⁴² In contrast, the band intensity of the thermally more stable polyethersulfone remains constant (see light gray area).⁴² With further rising temperature it is finally also degraded and no more infrared signal can be detected. If no infrared signal (ns) can be identified, the matrix is depleted, confirmed by the decomposition of both thermoset and thermoplastic. The intensities of the bands are determined by baseline-corrected integration. By comparing the intensity ratio of these both components, matrix degradation can be quantified.

Figure 4(b) visualizes this intensity ratio $I_d = I_{1510 \text{ cm}^{-1}}/I_{1486 \text{ cm}^{-1}}$ in relation to the ply depth p . The infrared intensity ratio is $I_d = 1.11 \pm 0.02$ in the initial state and drops with rising thermal loading. During one-sided thermal irradiation at high heat fluxes, extreme intensity ratio gradients occur along the specimen cross-section. Similar to the structural damage distribution investigated by μCT , I_d gradients can be separated into three regions. Beginning from the specimen back side ($p = 32$), the virgin r_{III} , matrix degraded r_{II} and matrix depleted r_{I} regions appear. In region r_{III} , the intensity ratio remains almost on the initial level. Only in r_{II} , the intensity ratio drops significantly due to epoxy resin decomposition. Thereby, the matrix is sufficiently damaged that thermo-induced delaminations occur as determined by μCT . The transition from r_{III} to r_{II} thus

represents the threshold for delamination formation at $I_d = 0.94 \pm 0.07$. A slight deviation from the previously reported threshold value of 0.79 ± 0.04 ¹⁵ is explained by the different integration method and the higher heat flux level of 50 W/cm^2 compared to 5 W/cm^2 . Based on this threshold, the depth where structural damage occurs can also be found with FTIR. In the matrix depleted region r_I , no infrared signal $I_d = \text{ns}$ can be detected anymore, due to additional decomposition of the polyethersulfone. These depths at $I_d = \text{ns}$ consequently represent the

border for matrix depletion at $A_d/A_0 = 20 \pm 5\%$ in Figure 3(b). Now the 32 plies of the irradiated specimen can be allocated to the three regions. When composites are thermally irradiated for, e. g., $t_i = 10 \text{ s}$, the cross-section can be divided in 22 virgin, four degraded and six depleted plies by FTIR. With rising thermal exposure, the virgin plies get more and more reduced. Simultaneously, matrix degraded and depleted plies increase until ultimately all plies are depleted.

As described previously, the three damage regions can be classified with μCT and FTIR. For visualization, Figure 5 represents the damage region sizes depending on the irradiation time t_i for both methods. Thereby, the regions are delimited regarding the depth and separated as follows: Beginning from the back side, the virgin region r_{III} appears without structural damage and infrared intensity ratios of $I_d > 0.94 \pm 0.07$. As soon as structural damage such as delaminations, pores and cracks become visible, region r_{II} is present. In region r_I , the matrix is additionally depleted, resulting at $A_d/A_0 \geq 20 \pm 5\%$ or $I_d = \text{ns}$. Thus, for undamaged materials, all 32 plies can be assigned to the virgin region r_{III} . Only with rising thermal exposure, region r_{II} with structural damage and r_I with matrix depletion arise. Simultaneously, the size of region r_{III} decreases until it no longer exists from $t_i \geq 25 \text{ s}$. Thereby, the assigned region ply numbers are similar between μCT and FTIR. The error from r_{III} to r_{II} and from r_{II} to r_I is only ± 1 ply between the two methods. Consequently, both non-destructive measurement methods can be used independently to separate the specimen cross-section into the three damage regions.

Furthermore, the matrix damage of CFRP can be mechanically characterized by means of DMA.²⁷ For this purpose, the storage modulus $G'(T)$ from bulk samples at various irradiation times t_i is shown in Figure 6(a). With

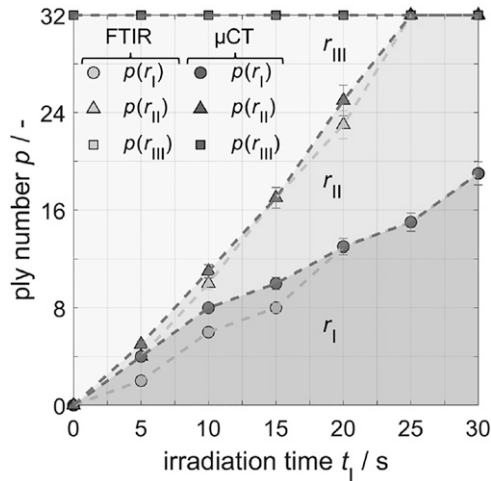


Figure 5. Identification of damage regions using μCT and FTIR: Ply number p without structural damage is represented by $p(r_{III,\mu\text{CT}})$ and $p(r_{III,\text{IR}})$, structural damage by $p(r_{II,\mu\text{CT}})$ and $p(r_{II,\text{IR}})$ as well as matrix depletion by $p(r_{I,\mu\text{CT}})$ and by $p(r_{I,\text{IR}})$ versus irradiation time t_i .

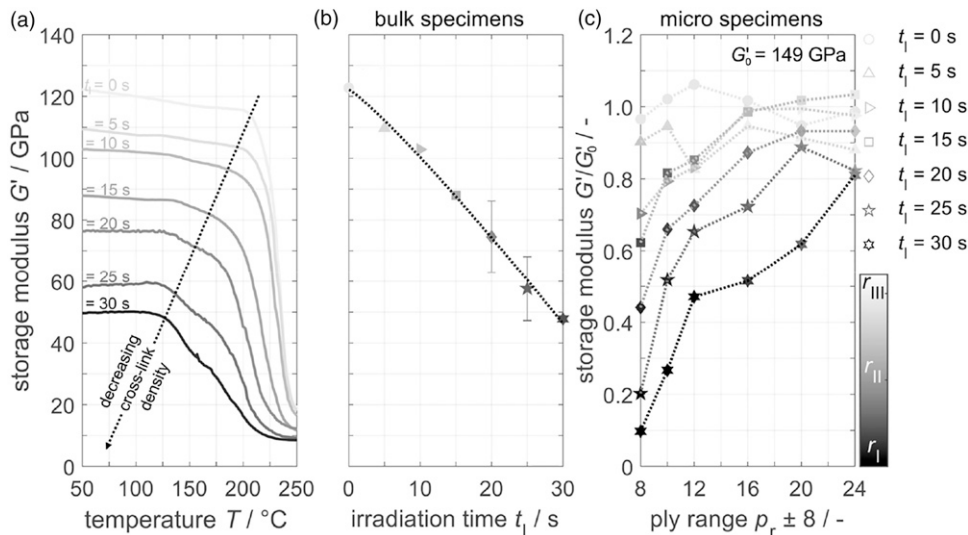


Figure 6. Determination of storage modulus depending on (a) temperature $G'(T)$ at different irradiation times t_i as well as (b) irradiation time $G'(t_i)$ from energy-elastic range at $T = 50 \text{ }^\circ\text{C}$ of bulk specimens recorded by DMA. Furthermore, depth profiles of (c) normalized storage modulus G'/G'_0 versus ply range p_r of micro specimens with damage regions r_i are visualized.

rising temperature, the transition from energy-elastic to entropy-elastic behavior is reflected in the drop of the storage modulus. For the non-thermally pre-loaded material, the glass transition temperature is $T_g = 232 \text{ }^\circ\text{C}$, determined by the inflection point of the $G'(T)$ curve. In case of thermally pre-damaged specimens, the inflection points shift to lower temperatures and storage moduli. These developments can be attributed to increased mobility and flexibility of the molecular fragments, caused by, e. g., cracks in epoxy resin macromolecules.^{43,44} As a result, the stiffness of the material reduces. Since the cross-link density correlates with the storage modulus, stiffness drop can be used to quantify the matrix damage.^{43,44} For illustration, Figure 6(b) shows the storage modulus $G'(t)$ at $T = 50 \text{ }^\circ\text{C}$. With rising irradiation time, the storage modulus of the bulk samples drops because the damage accumulates within the matrix. The corresponding depth profiles are illustrated in Figure 6(c) as normalized storage modulus versus ply ranges p_r for micro samples. In case of one-sided thermal loads, stiffness gradients arise along the cross-section, affected differently by the thermo-induced damage. Beginning from the back side ($p = 32$), the in light gray visualized region r_{III} without structural damage hardly reduces the stiffness. Only with defects in r_{II} (dark gray) and especially with matrix depletion in r_I (black) the stiffness drops significantly. Consequently, the damage regions are also reflected in the material stiffness and matrix damage.

In summary, using DMA, FTIR and μCT , matrix damage can be characterized volumetrically via material stiffness, matrix degradation locally along the cross-section and structural damage within the material. Thereby, the methods complement each other optimally to explain the thermo-induced damage comprehensively by the three defined damage regions r_{III} , r_{II} and r_I .

Mechanical properties

In the following, the impact of thermo-induced damage in irradiated composites on mechanical properties is

characterized. Thereby, the resulting damage phenomena for non-irradiated and irradiated bulk specimens in short beam shear, compressive, flexural and tensile tests are analyzed in Table 3. During mechanical loading of specimens with increasing thermal damage, the failure phenomena can change. For example, the tensile specimens show with declining fibre-matrix bonding, no smooth cracks, but fractures with brooming.^{35,45,46} Similarly for compressive samples, the damage phenomenon changes from compressive failure to buckling caused by brooming.^{32,45,46} If extreme damage distribution along the cross-section exist, as it is the case in one-sided thermally loaded specimens with high heat fluxes, combined fractures can occur.¹⁴

During short beam shear and four-point flexural test, the specimens are loaded under tensile, compressive and shear stress. Since in the short beam shear test small length to thickness ratios of the specimens are used, shear stresses dominate in the material.^{31,45,46} With progressive damage, the phenomenon changes from shear failure in one or more plies with brittle behavior to shear failure in multiple plies with ductile behavior. Under mechanical loading, shear failure with brittle behavior is indicated by steep stress-per-strain rise and significant drop at maximum force. As a result, at least one ply delaminates, which is macroscopically visible in Table 3. In comparison, shear failure with ductile behavior is indicated by flat stress-per-strain rise with multiple small stress drops and higher strains. Thereby, no significant stress drop occurs anymore due to the thermo-induced low interlaminar adhesion between the plies. For both phenomena, the first force drop is evaluated to calculate the apparent interlaminar shear strength because this is the initial point of failure.³¹ In the four-point flexural test, compressive and tensile stresses dominate. Thereby, with rising thermal damage, the behavior can change from compressive to tensile failure caused by brooming.^{34,45,46} Thus, the damage states within the specimens are reflected

Table 3. Photographs of typical damage phenomena in short beam shear, compressive, four-point flexural and tensile tests for non-irradiated and irradiated bulk specimens.

	Short beam shear test	Compressive test	Four-point flexural test	Tensile test
Non-irradiated	 Shear failure/brittle	 Compressive failure	 Compressive failure	 crack
Irradiated	 Shear failure / ductile (25 s)	 Brooming / comp. Fail. (15 s)	 Brooming / comp. Fail. (30 s)	 Brooming / crack (30 s)

in the failure phenomena and consequently in the mechanical properties.

Figure 7 shows the mechanical properties of the normalized interlaminar shear, compressive, flexural and tensile strength of (a–d) bulk and (e–h) micro specimens. The depth-resolved strength evolution induced by one-sided thermal loading can be directly analyzed by micro samples prepared from bulk material. Consequently, for non-irradiated bulk and micro specimens, similar interlaminar shear strengths of $\tau_0 = 114 \pm 2$ MPa and $\tau_0 = 120 \pm 2$ MPa, respectively, are obtained because in the short beam shear test the support sizes and distances are changed by a defined factor. With rising thermal loading, the strength of the specimens decreases

as expected. For example, at $q = 50$ W/cm² and $t_1 = 5$ s, residual strengths decrease for interlaminar shear strength to $\tau/\tau_0 = 0.81$, compressive strength to $\sigma_c/\sigma_{c,0} = 0.86$, flexural strength to $\sigma_f/\sigma_{f,0} = 0.87$ and tensile strength to $\sigma_t/\sigma_{t,0} = 0.96$ for the bulk material. Thus, after thermal loading, interlaminar shear strength reacts most sensitive to the irradiation scenario, followed by compressive, flexural and finally tensile strength. The effect of thermo-induced damage on mechanical strength along the cross-section can be taken from the depth profiles in (e–h). In this consideration, the virgin region r_{III} (light gray) has only a minor influence on the mechanical properties because its corresponding residual strengths hardly differ from the initial strengths. Only

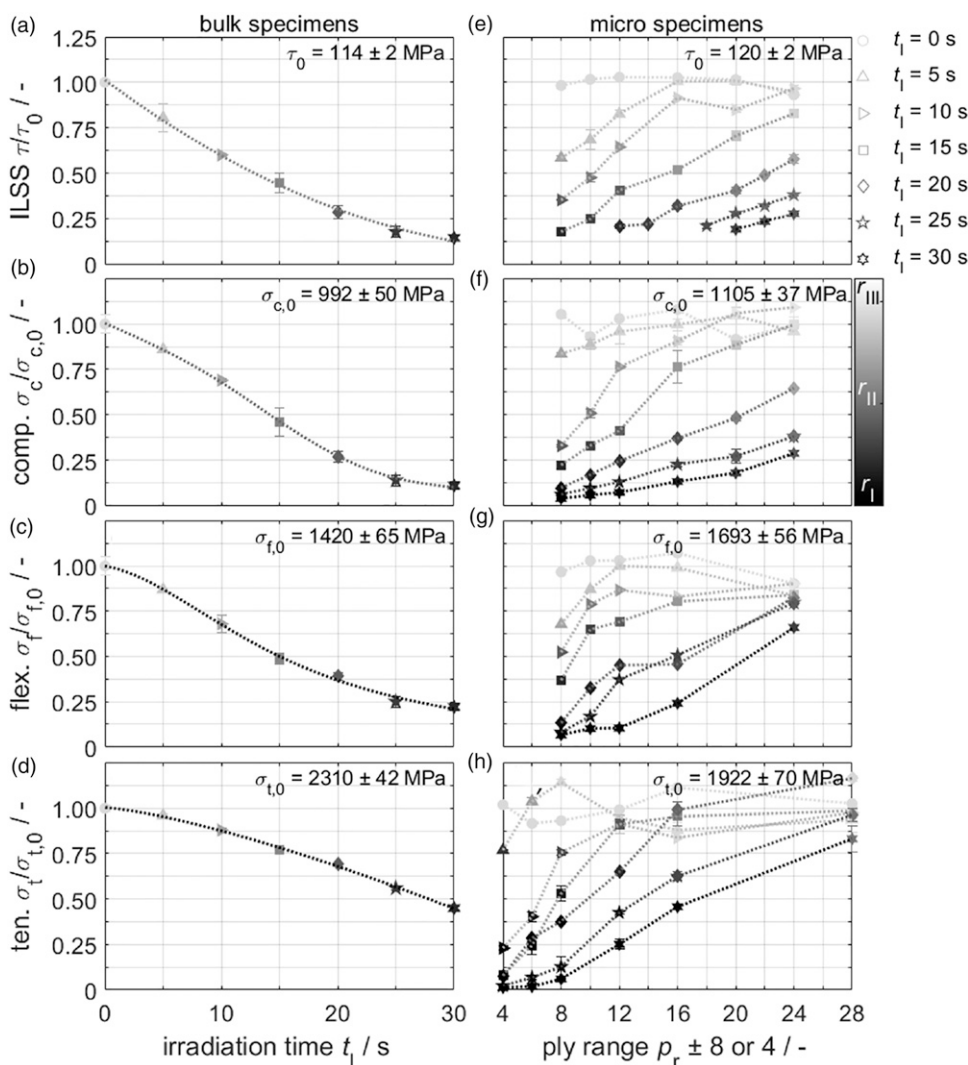


Figure 7. Comparison of mechanical properties between bulk and micro specimens for normalized (a, e) interlaminar shear strength τ/τ_0 , (b, f) compressive strength $\sigma_c/\sigma_{c,0}$, (c, g) flexural strength $\sigma_f/\sigma_{f,0}$ and (d, h) tensile strength $\sigma_t/\sigma_{t,0}$ depending on irradiation time t_1 and ply range $p_r \pm 8$ for (e–g) and $p_r \pm 4$ for (h). In addition, the initial strengths of bulk material and damage regions r_i are shown.

with the presence of structural damage (dark gray), noticeable strength drops occur. When the matrix is additionally depleted (black), extreme strength losses result for all mechanical loading types. For visualization, Table 1 summarizes the damage region sizes, ply ranges and failure phenomena. When these are compared, a correlation between region r_I and brooming becomes evident. During compressive, flexural and tensile loads, brooming occurs only in ply ranges with region r_I . This indicates that brooming requires a matrix degradation of $I_d = ns$ or structural damage of at least $A_d/A_0 \geq 20 \pm 5\%$.

To determine the effect of structural damage on mechanical properties, the interlaminar shear, compressive, flexural and tensile strength are correlated with the

normalized damaged sample volume V_d/V_0 in Figures 8(a)–(d). Generally, with rising structural damage in the specimen, the strength declines. Since the residual strength decreases approximately linearly between $V_d/V_0 = 0$ and 0.01, the sensitivity of the strength types to thermo-induced damage can be expressed via the line slope m . For example, in this range, the slope flattens from interlaminar shear strength with $m(\tau/\tau_0) = -30.6 <$ compressive strength with $m(\sigma_c/\sigma_{c,0}) = -20.8 <$ flexural strength with $m(\sigma_f/\sigma_{f,0}) = -3.9 <$ tensile strength with $m(\sigma_t/\sigma_{t,0}) = -3.0$. The closer the slope is to 0, the lower is the effect of thermo-induced damage on the strength types. Thus, interlaminar shear and compressive strength are most affected by minor structural damage. In the compressive test, defects parallel to the mechanical

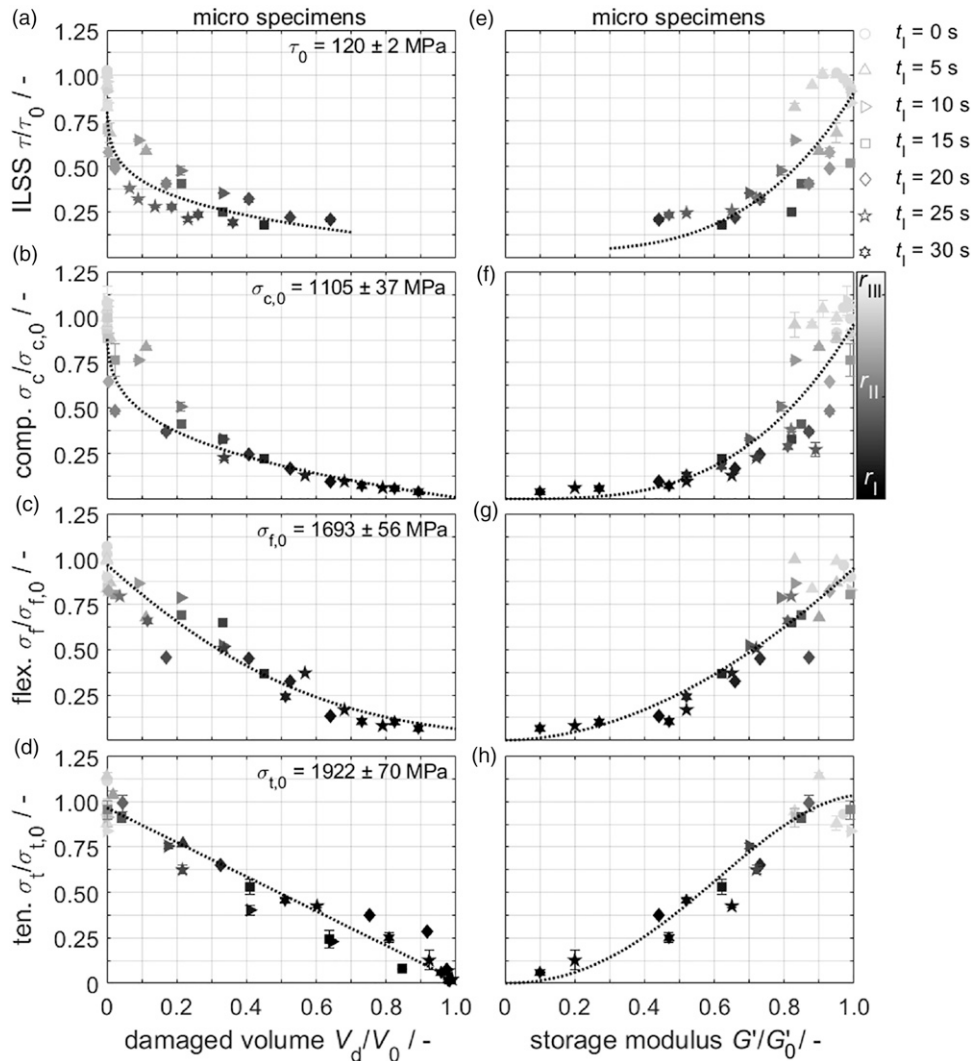


Figure 8. Comparison of damaged volume V_d/V_0 determined by μ CT and normalized storage modulus G'/G'_0 evaluated by DMA with normalized (a, e) interlaminar shear strength τ/τ_0 , (b, f) compressive strength $\sigma_c/\sigma_{c,0}$, (c, g) flexural strength $\sigma_f/\sigma_{f,0}$ and (d, h) tensile strength $\sigma_t/\sigma_{t,0}$ of micro specimens. In addition, the initial strengths of micro specimens and damage regions r_i are presented.

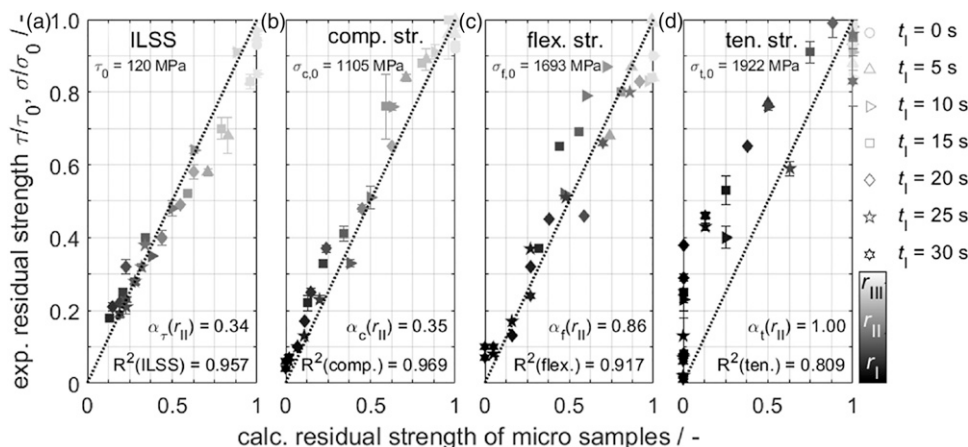


Figure 9. Comparison between experimental and calculated residual (a) interlaminar shear τ/τ_0 , (b) compressive $\sigma_c/\sigma_{c,0}$, (c) flexural $\sigma_f/\sigma_{f,0}$ and (d) tensile strength $\sigma_t/\sigma_{t,0}$ of micro samples. The calculated strengths are obtained with constant $\alpha(r_{II}) = 1$, $\alpha(r_I) = 0$ as well as variable $0 < \alpha(r_{II}) < 1$ sensitivity factors using Formula (1). In addition, coefficients of determination R^2 and damage regions r_i are illustrated.

loading direction can lead to facilitated separation of fibre and matrix and thus to premature failure.⁴⁶ In contrast, flexural and especially tensile strength are hardly impaired. Since in the 0° tensile test the composite strength is dominated by fibre strength, this mechanical loading type is least sensitive to matrix depletion at low damaged volume.⁴⁶

Furthermore, the influence of matrix damage on mechanical properties can be identified by correlating the interlaminar shear, compressive, flexural and tensile strength with the normalized storage modulus G'/G'_0 in Figures 8(e)–(h). Similar to the damaged volume, the sensitivity of the strength types to matrix damage can be expressed by the approximated line slope between $G'/G'_0 = 1$ and 0.9. The slope drops from interlaminar shear strength with $m(\tau/\tau_0) = 3.6 >$ compressive strength with $m(\sigma_c/\sigma_{c,0}) = 3.1 >$ flexural strength with $m(\sigma_f/\sigma_{f,0}) = 2.2 >$ tensile strength with $m(\sigma_t/\sigma_{t,0}) = 0.2$. Obviously, the matrix damage affects the interlaminar shear strength most followed by the compressive strength. In the short beam shear test, moderate degradation of polymeric matrix already impairs the residual strength due to weakening of interlaminar adhesion. Flexural strength is slightly and tensile strength hardly affected by low matrix damage. For significant tensile strength loss, matrix depletion or carbon fibre degradation must be present. Consequently, the strength loss begins approximately at the decomposition temperature of the polyethersulfone at 510°C ¹⁴ and carbon fibre at 608°C ,¹⁴ respectively, determined by thermogravimetric analysis at $10^\circ\text{C}/\text{min}$ under oxygen atmosphere. The explicit contribution of the various damage effects to the sensitivity of different strength types can be quantified by a three-region model.

Three-region model for strength calculation

In the following, the three-region model is introduced to predict the mechanical properties of CFRP after one-sided thermal irradiation based on the thermo-induced damage distribution in the material. For this purpose, the sample cross-section is separated into three damage regions defined by non-destructive methods such as μCT in Figure 3(b) or FTIR in Figure 4(b). Subsequently, the ply numbers of the regions $p(r_i)$ are determined and normalized to the total ply number p_t . Finally, the normalized residual strength τ_{rs}/τ_0 is calculated from the product sum of relative region sizes $p(r_i)/p_t$ and sensitivity factors $\alpha(r_i)$ according to Formula (1).

$$\tau_{rs}/\tau_0 = \left[\left(\frac{p(r_{III})}{p_t} \right) \cdot \alpha(r_{III}) + \left(\frac{p(r_{II})}{p_t} \right) \cdot \alpha(r_{II}) + \left(\frac{p(r_I)}{p_t} \right) \cdot \alpha(r_I) \right] \quad (1)$$

The sensitivity factors represent the different impact of the damage regions r_{III} , r_{II} and r_I on the various types of mechanical loading. Thereby, the factors can reach values between 0 (no residual strength left) and 1 (initial strength). Consequently, from the virgin region r_{III} to matrix depleted region r_I , the sensitivity factor declines. As first approximation, sensitivity factors of $\alpha(r_{III}) = 1$ and $\alpha(r_I) = 0$ can be selected for all strength types. This means that the strength does not decrease at region r_{III} and completely at region r_I . The sensitivity factors for region r_{II} are intermediate and can be calculated using the least square method^{47–49}. In this method, the factor is adjusted until the residual sum of squares from calculated and experimental values reaches a minimum. For illustration, Figures 9(a)–(d) shows the experimental residual strengths versus the calculated residual strengths according to

Formula (1) for interlaminar shear, compressive, flexural and tensile strength. Thereby, the experimental strengths of the micro samples are used to calibrate the sensitivity factors. The approximation results in low sensitivity factors for interlaminar shear strength with $\alpha_c(r_{II}) = 0.34$ and compressive strength with $\alpha_c(r_{II}) = 0.35$ and higher factors for flexural strength with $\alpha_f(r_{II}) = 0.86$ and tensile strength with $\alpha_t(r_{II}) = 1.00$. Thus, the effect of structural damage in region r_{II} on mechanical properties decreases from interlaminar shear to compressive, flexural and tensile strength. The sensitivity sequence is consistent with the determined line slopes in Figures 8(a)–(d). Consequently, the sensitivity factors correlate with the corresponding damage regions. With known initial strengths, region sizes and sensitivity factors, the residual strengths can now be calculated. As an example, for interlaminar shear strengths, intensity factors of $\alpha_c(r_{III}) = 1$, $\alpha_c(r_{II}) = 0.34$, and $\alpha_c(r_I) = 0$ are applied. If the micro sample is composed of $p(r_{III}) = 7$, $p(r_{II}) = 3$ and $p(r_I) = 6$ plies, a residual strength of $\tau_{rs} = 60$ MPa is calculated, which corresponds to the experimental residual strength of $\tau = 57 \pm 3$ MPa. For the various strength types, the coefficients of determination between experimental and calculated strengths are $R^2(\text{ILSS}) = 0.957$, $R^2(\text{comp.}) = 0.969$, $R^2(\text{flex.}) = 0.917$, $R^2(\text{ten.}) = 0.809$. Thus, the assumption of $\alpha_c(r_{III}) = 1$ and $\alpha_c(r_I) = 0$ for the sensitivity factors provides a good prediction quality for interlaminar shear, compressive and flexural strength. In comparison, the calculated tensile strength deviates most from the experimental values, which can be attributed to a systematic error of the sensitivity factors.

The assumptions that region r_{III} leads to no and region r_I to complete strength loss are simplifications which can be more accurately determined on the basis of the generated results. For this purpose, the correlation of residual strength with damaged volume and storage modulus in Figure 8 also considers the effect of damaged regions on mechanical properties using gray value scaling. The strength values for region r_{III} (light gray) are near $V_d/V_0 \sim 0$ and $G'/G'_0 \sim 1$, respectively. It is obvious that the strength values of region r_{III} might be significantly lower than the initial strengths. Thereby, the reduced strengths can be attributed to the weakening of the fibre-matrix adhesion and matrix degradation without visible structural damage. The steeper the line slopes from strength progression depending on the damaged volume and stiffness, the more sensitive the strength type reacts to the damage region r_{III} . Since the line slope flattens from interlaminar shear to compressive, flexural and tensile strength, the strength types are less affected by moderate matrix degradation in this sequence. For this reason, the sensitivity factors $\alpha(r_{III})$ are not necessarily 1 as previously assumed, but can be slightly lower. Similarly for region r_I (black), when the matrix is depleted, the material may still retain very low residual strengths. Thus, the

sensitivity factors for the first region are not necessarily 0, but can be slightly higher.

For these reasons, all sensitivity factors in the advanced three-region model are adjusted using the least-square method^{47–49}. For example, interlaminar shear strength provides sensitivity factors of $\alpha_c(r_{III}) = 0.94$, $\alpha_c(r_{II}) = 0.32$ and $\alpha_c(r_I) = 0.04$. If the micro sample is composed of $p(r_{III}) = 7$, $p(r_{II}) = 3$ and $p(r_I) = 6$ plies, a residual strength of $\tau_{rs} = 58$ MPa is calculated, which corresponds to the experimental strength of $\tau = 57 \pm 3$ MPa. Thereby, between the experimental residual strengths and calculated strengths of micro specimens, the coefficients of determination are $R^2(\text{ILSS}) = 0.967$, $R^2(\text{comp.}) = 0.970$, $R^2(\text{flex.}) = 0.927$, $R^2(\text{ten.}) = 0.850$. Thus, good prediction quality is available for all strength types. A summary of all sensitivity factors is given in Table 4.

To evaluate the sensitivity factors, the experimental residual strengths are compared to the calculated residual strengths of the bulk material using (a) three-region model and (b) advanced three-region model in Figure 10. In the three-region model, the sensitivity factors $\alpha(r_{III}) = 1$ and $\alpha(r_I) = 0$ are set constant for simplification and only $\alpha(r_{II})$ is varied. In contrast, in the advanced three-region model, all factors are adjusted according to the determined strength type sensitivities to thermo-induced damage. For both models, the prediction quality is high with $R^2 = 0.964$ and $R^2 = 0.983$, respectively, for all strength types of the bulk samples. For interlaminar shear, compressive and flexural strength, both models are equivalent since the sensitivity factors are similar. These strength types are hardly affected by region r_{III} with moderate matrix degradation and extremely by region r_I with matrix depletion. Thus, the strength types differ primarily in their different sensitivities to region r_{II} with delaminations. For the determination of tensile strength, the simple-region model provides good $R^2(\text{ten.}) = 0.881$ and the advanced excellent $R^2(\text{ten.}) = 0.940$ accuracies. This is because region r_I must not lead to complete strength loss according to the sensitivity factor of $\alpha_t(r_I) = 0.3$. Consequently, for a precise calculation of the tensile strength of severely damaged specimens $\sigma_v/\sigma_{t,0} < 0.3$,

Table 4. Overview of sensitivity factors $\alpha(r_i)$ from the simple and advanced 3-region model for interlaminar shear, compressive, flexural, and tensile strength.

Strength type	Sensitivity factors of 3-region model / -			Sensitivity factors of advanced 3-region model / -		
	$\alpha(r_{III})$	$\alpha(r_{II})$	$\alpha(r_I)$	$\alpha(r_{III})$	$\alpha(r_{II})$	$\alpha(r_I)$
Int. Shear strength	1.00	0.34	0.00	0.94	0.32	0.04
Compressive strength	1.00	0.35	0.00	0.98	0.34	0.04
Flexural strength	1.00	0.86	0.00	0.99	0.78	0.08
Tensile strength	1.00	1.00	0.00	1.00	0.85	0.30

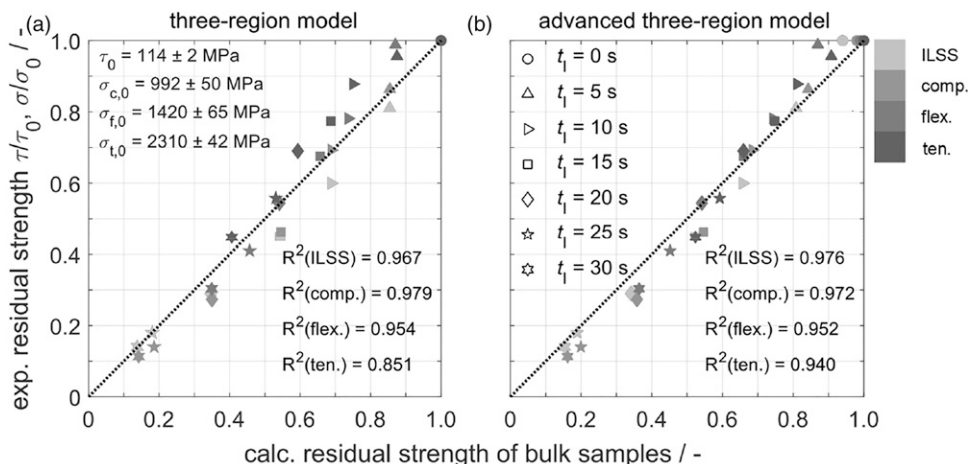


Figure 10. Comparison of experimental and calculated residual strengths of bulk specimens using (a) three-region model and (b) advanced three-region model. In addition, coefficients of determination R^2 are given to illustrate the prediction quality.

a fourth region r_{IV} with fibre degradation might be introduced in a further advanced model.

Compared to other approaches,^{18,50} the three-region model is characterized by the following features: Since the material cross-section is divided into three damage regions, the model provides an excellent approximation of strength. Furthermore, it is not necessary that irradiation conditions as well as radiation effects must be known, because only the distribution of the three regions is considered. Moreover, the model can be used to predict the mechanical properties of various strength types. Thereby, the influence of strength types on thermo-induced damage can be expressed with sensitivity factors. The material thickness and expansion in the z -direction may be negligible due to the ply-related approach. However, depth-resolved investigations require considerable instrumental effort.

Conclusion

In this work, the CFRP 8552/IM7 was thermally loaded from one side at $q = 50$ W/cm² under varying irradiation times. The temperature was recorded depending on exposure time and ply position. Subsequently, defined plies of bulk material were removed to prepare micro samples from different depths. Both bulk and micro samples were examined by non-destructive and destructive methods.

During one-sided thermal loading, the material heats up under formation of temperature gradients along the thickness direction. As a result, damage gradients develop, which can be generally divided into three regions using non-destructive methods like μ CT and FTIR. Beginning from the back side, in region r_{III} , no visible structural damage can be detected. Nevertheless, moderate weakening of fibre-matrix adhesion and matrix degradation may be present. In contrast, region r_{II} contains structural damage such as

delaminations, cracks and pores. In region r_I , the matrix is additionally depleted and carbon fibres are set free.

Thereby, μ CT and FTIR are differently sensitive to thermal damage of CFRP. Whereas, FTIR is able to detect moderate thermal damage such as matrix degradation, μ CT is limited to more pronounced structural damage. However, both methods are suitable to identify the three damage regions. FTIR can characterize the transition from virgin to structural damage region ($r_{III} \rightarrow r_{II}$) by the threshold for delamination formation. While μ CT identifies the transition between structural damage to matrix depleted region ($r_{II} \rightarrow r_I$) by the threshold for matrix depletion. Thus, both methods complement each other optimally and can be used independently within this study.

By ply-dependent characterization of thermal degradation in composites, the influence of heat flux, decomposition processes and damage regions on residual strength can be determined. It turns out that the damage regions from moderate matrix degradation, via structural damage to matrix depletion increasingly affect the strengths. Thereby, interlaminar shear is affected most, followed by compressive, flexural and tensile strength. Tensile strength in fibre direction is least sensitive to heat flux and irradiation time, since matrix depletion or fibre decomposition must be present for a significant strength drop. If matrix depletion is present, brooming occurs and thus failure phenomena during mechanical loading change.

It is important to consider the various steps of the degradation mechanism with respect to their different impact on the four investigated strength types. By this, it is possible to correlate the expansion of the three regions, in which the various degradation steps differently occur, with the residual strength, separately for interlaminar shear, compressive, flexural and tensile strength. Based on these

findings, a three-region model can be introduced to predict the mechanical properties of thermally loaded composites. In this model, the material cross-section is divided into three damage regions and the residual strength is calculated from the product sum of initial strengths, relative region sizes and sensitivity factors. The sensitivity factors represent the influence of damage regions and therefore the effect of the certain degradation steps on the various strength types. For the simple model, the assumptions are made that the strength types are not affected by virgin region and maximally influenced by matrix depleted region. Thus, the influence of structural damage to strength types can be quantified. In the advanced model, all sensitivity factors are adjusted according to the quantification of thermal damage in CFRP. Thereby, both models provide excellent prediction qualities for interlaminar shear, compressive and flexural strength. Moreover, in the advanced model, the predicted tensile strengths are more accurate, since matrix depletion does not necessarily lead to complete strength loss.

The overall goal of this work is to use non-destructive methods in combination with the three-region model to characterize, classify and quantify the thermo-induced damage in CFRP components after real thermal loading scenarios in order to predict its residual strengths. To realize this, the model will still be validated in future research for different irradiation scenarios like long-lasting low heat fluxes and short-lasting high heat fluxes, various material thicknesses and materials types. Based on these results, the model should be universally applicable for even unknown irradiation conditions and common materials with different laminate structures. Furthermore, the damage regions will be correlated with temperature profiles to find possible temperature thresholds for damage processes. As a result, maximum material temperatures could also be inferred from thermo-induced damage. Finally, the presented results might also be a good basis for refined finite element simulations, considering the thresholds for various damage states.

Acknowledgements

The authors want to thank André Ehgartner for his experimental support.

Declaration of conflicting interests

The author(s) declared no potential conflicts of interest with respect to the research, authorship, and/or publication of this article.

Funding

The author(s) disclosed receipt of the following financial support for the research, authorship, and/or publication of this article: We acknowledge financial support for open access publication by SAGE Choice of the Universität der Bundeswehr München.

ORCID iDs

Johannes Bibinger  <https://orcid.org/0000-0003-4001-5496>

Sebastian Eibl  <https://orcid.org/0000-0003-0915-3022>

References

1. Soutis C. Carbon fiber reinforced plastics in aircraft construction. *Mater Sci Eng A* 2005; 412: 171–176.
2. Clyne TW and Hull D. *An introduction to composite materials*. 3rd ed. Cambridge University Press, 2019.
3. Schürmann H. *Konstruieren mit Faser-Kunststoff-Verbunden*. 2nd ed. Springer Berlin Heidelberg, 2007.
4. Eurofighter Jagdflugzeug GmbH. *Technical guide - Eurofighter typhoon*. www.eurofighter.com (2013, accessed 7 April 2020).
5. Neitzel M, Breuer U and Mitschang P. *Handbuch Verbundwerkstoffe - Werkstoffe, Verarbeitung, Anwendung*. 2nd ed. Carl Hanser Verlag, 2014.
6. Sauer M, Kühnel M and Witten E. *Report - Composites market report 2018 - Market developments, trends, outlook and challenges*. www.carbon-connected.de (2018, accessed 7 April 2020).
7. Azwa ZN and Yousif BF. Characteristics of kenaf fibre/epoxy composites subjected to thermal degradation. *Polym Degrad Stab* 2013; 98: 2752–2759.
8. Naruse T, Hattori T, Miura H, et al. Evaluation of thermal degradation of unidirectional CFRP rings. *Compos Struct* 2001; 52: 533–538.
9. Ohno S, Lee M, Lin KY, et al. Thermal degradation of IM7/BMI5260 composite materials: characterization by X-ray photoelectron spectroscopy. *Mater Sci Eng A* 2000; 293: 88–94.
10. Ray S and Ralph P. *Handbook of environmental degradation of materials*. 3rd ed. Elsevier Inc., 2018.
11. Trelles J and Lattimer BY. Modelling thermal degradation of composite materials. *Fire Mater* 2007; 31: 147–171.
12. Scharfel B and Hull TR. Development of fire-retarded materials - Interpretation of cone calorimeter data. *Fire Mater* 2007; 31: 327–354.
13. Mclean AD. Burns and Military Clothing. *J R Army Med Corps* 2001; 147: 97–106.
14. Bibinger J, Eibl S and Gudladt H-J. Influence of low and extreme heat fluxes on thermal degradation of carbon fibre-reinforced polymers. *Appl Compos Mater* 2022; 29: 1817–1840.
15. Vetter T, Bibinger J, Zimmer F, et al. Characterization of one-sided thermal damage of carbon fiber reinforced polymers by means of depth profiles. *J Compos Mater* 2020; 54: 3699–3713.
16. Eibl S. Influence of unwoven roving and woven fabric carbon fiber reinforcements on reaction-to-fire properties of polymer matrix composites. *Fire Mater* 2020; 44: 557–572.
17. Swanson D and Wolfrum J. Time to failure modeling of carbon fiber reinforced polymer composites subject to simultaneous tension and one-sided heat flux. *J Compos Mater* 2018; 52: 2503–2514.

18. Mouritz AP, Feih S, Kandare E, et al. Review of fire structural modelling of polymer composites. *Compos A* 2009; 40: 1800–1814.
19. Hexcel Composites. *Datasheet - HexPly® 8552, epoxy matrix (180 °C/356 °F curing matrix)*., www.hexcel.com (2016, accessed May 12, 2020).
20. Hexcel Corporation. *Datasheet - HexTow® IM7 carbon fiber*., www.hexcel.com (2018, accessed April 9, 2020).
21. Eibl S. Observing Inhomogeneity of Plastic Components in Carbon Fiber Reinforced Polymer Materials by ATR-FTIR Spectroscopy in the Micrometer Scale. *J Compos Mater* 2008; 42: 1231–1246.
22. Dao B, Hodgkin J, Krstina J, et al. Accelerated Aging Versus Realistic Aging in Aerospace Composite Materials . II. Chemistry of Thermal Aging in a Structural Composite. *J Appl Polym Sci* 2006; 102: 3221–3232.
23. Hexcel Composites. *Datasheet - Hexcel® HexPly® 8552 epoxy matrix, IM7 fiber 2022*, www.lookpolymers.com (accessed on 19 January 2022).
24. Thermodirekt. *Datasheet - Thermoleitung für Thermoelementfühler*, www.thermodirekt.de (accessed 27 April 2020).
25. DIN EN ISO 16810. *Non-destructive testing - Ultrasonic testing; German version*. Beuth Verlag Berlin, 2014.
26. Eibl S. Reliable and universally applicable chemometric techniques based on infrared spectroscopy to non-destructively quantify thermal damage of carbon fibre reinforced epoxy matrix composites. *Polym Test* 2019; 76: 396–410.
27. DIN EN ISO 6721-1. *Determination of dynamic mechanical properties - Part 1: General principles; German version*. Beuth Verlag Berlin, 2018.
28. DIN EN ISO 1183-1. *Methods for determining the density of non-cellular plastics - Part 1: immersion method, liquid pycnometer method and titration method; German version*. Beuth Verlag Berlin, 2019.
29. Elhajjar R, Grant P and Ashforth C. *Composite structures: effects of defects*. 1st ed. John Wiley & Sons, 2018.
30. Krenkel W. *Ceramic matrix composites*. 1st ed. Wiley-VCH Verlag GmbH, 2008.
31. DIN EN 2563. *Carbon fibre reinforced plastics - unidirectional laminates - determination of the apparent interlaminar shear strength; German version*. Beuth Verlag Berlin, 1997.
32. DIN EN ISO 14126. *Determination of compressive properties in the in-plane direction; German version*. Beuth Verlag Berlin, 2000.
33. DELO Industrie Klebstoffe GmbH. *Datasheet - DELO-DUPOX® 1895*., www.hillmann-geitz.de (2013, accessed May 2, 2020).
34. DIN ENISO 14125. *Determination of flexural properties; German version*. Beuth Verlag Berlin, 2011.
35. DIN EN 2561. *Tensile test parallel to the fibre direction; German version*. Beuth Verlag Berlin, 1995.
36. Howell JR and Pinar Mengüç M *Thermal radiation heat transfer*. 6th ed. Taylor & Francis, 2016.
37. Hahn DW and Özisik MN. *Heat conduction*. 3rd ed. John Wiley & Sons, 2012.
38. von Böckh P and Stripf M. *Technische thermodynamik*. 2nd ed. Springer Vieweg, 2015.
39. von Böckh P and Wetzel T. *Wärmeübertragung*. 4th ed. Springer Berlin Heidelberg, 2011.
40. Faghri M and Sundén B. *Transport phenomena in fires*. 1st ed. WIT Press, 2008.
41. O’Gorman L, Sammon MJ and Seul M. *Practical algorithms for image analysis*. 2nd ed. Cambridge University Press, 2008.
42. Wolfrum J, Eibl S and Lietch L. Rapid evaluation of long-term thermal degradation of carbon fibre epoxy composites. *Compos Sci Technol* 2009; 69: 523–530.
43. Nielsen LE and Landel RF. *Mechanical properties of polymers and composites*. 2nd ed. Taylor & Francis, 1993.
44. Riande E, Díaz-Calleja R, Prolongo MG, et al. *Polymer viscoelasticity: stress and strain in practice*. 1st ed.. Taylor & Francis, 1999.
45. Ehrenstein GW. *Faserverbund-kunststoffe*. 2nd ed. Carl Hanser Verlag, 2006.
46. Grellmann W and Seidler S. *Polymer testing*. 2nd ed. Carl Hanser Verlag, 2013.
47. Happach V. *Ausgleichsrechnung nach der Methode der kleinsten Quadrate*. 1st ed. Vieweg and Teubner Verlag, 1923.
48. Ludwig R. *Methoden der Fehler- und Ausgleichsrechnung*. 1st ed. Vieweg and Teubner Verlag, 1969.
49. Papula L. *Mathematik für Ingenieure und Naturwissenschaftler*. 7th ed. Springer Vieweg, 2016.
50. Lattimer BY and Ouellette J. Properties of composite materials for thermal analysis involving fires. *Compos A Appl Sci Manuf* 2006; 37: 1068–1081.